

Article

Idealized Simulations of City-Storm Interactions in a Two-Dimensional Framework

Jason Naylor

Department of Geography and Geosciences, University of Louisville, Louisville, KY 40292, USA;
jason.naylor@louisville.edu

Received: 29 May 2020; Accepted: 28 June 2020; Published: 2 July 2020



Abstract: Numerous studies have identified spatial variability in convective parameters such as rainfall totals and lightning flashes in the vicinity of large urban areas, yet many questions remain regarding the storm-scale processes that are altered during interaction with a city as well as which urban features are most responsible for storm modification. This study uses an idealized, two-dimensional cloud model to investigate structural and evolutionary changes in a squall line as it passes over a simplified representation of a large city. A parameter space exploration is done in which the parameters of the city—surface temperature and surface roughness length—are systemically increased relative to the region surrounding the idealized city. The resultant suite of simulations demonstrates that storm parameters such as vertical velocity, hydrometeor mass, upward mass flux, and buoyant accelerations are enhanced when the storm passes over the idealized city. No such enhancement occurs in the control simulation without an idealized city.

Keywords: storms; convection; urban; modeling

1. Introduction

Although comprising only a small percentage of the world's land use, urban areas contain the majority of the world's population. In the United States, 70% of the population currently resides in urbanized areas [1] and it is projected that 68% of the world's population will live in urban areas by 2050 [2]. Convective events that occur over dense, populous urban areas may expose a large number of people to hazards such as flash flooding, damaging wind, large hail, and tornadoes. For this reason, timely and accurate threat information must be communicated to residents of large cities. However, urban environments often present unique challenges to convective forecasters.

Large urban areas have been shown to alter the spatial distribution and intensity of convective rainfall around them [3–11], with the most commonly observed signal being enhanced rainfall downwind of the urban core. Urban-induced convective initiation is most commonly associated with relatively benign synoptic patterns [12–16] with the resultant thunderstorms typically being short-lived and posing minimal risk for development of convective hazards. However, there is increasing evidence that urban areas can impact organized storm systems and modify the distribution of convective hazards associated with those storms. Huff and Changnon [4] noted that, beginning in the late 1940s, the downwind region of St. Louis, MO experienced more frequent hail events relative to areas upwind and within St. Louis. Reames and Stensrud [17] found that the near-surface rotational and updraft characteristics of supercells are impacted by their proximity to a large urban area. Naylor and Sexton [18] analyzed National Weather Service warning products around several large metropolitan areas within the Midwestern United States. They found that, in most of the cities studied, storm-based severe thunderstorm and tornado warnings were more common on the downwind side of a particular city compared to the upwind side.

There also remains considerable uncertainty regarding which urban features are responsible for storm modification. Huff and Changnon [19] proposed four potential urban processes that may modify convective storms: (1) A thermal mechanism due to the presence of the urban heat island (UHI); (2) an increase in low-level turbulence due to flow obstruction; (3) microphysical modifications due to urban aerosol emissions; and (4) modification of atmospheric moisture content. Various modeling and observational studies have attributed each of these mechanisms to convective variability in some way. Low-level convergence zones induced by the UHI have been associated with areas of frequent convective initiation [20,21]. Surface roughness gradients have been attributed to convergence zones and have been linked to storm bifurcation [22] and downwind enhancement of convective precipitation [23]. Urban aerosols have been shown to play a substantial role in urban storm modification [24–26], while spatial gradients in surface moisture over urban areas have also been shown to have an impact [27].

In a real-world setting, it is difficult to isolate these various mechanisms. Idealized storm-scale models allow for controlled variability in the parameters of interest and have been successfully used in the past to investigate the behavior of deep convective storms in particular environments [28–33]. The purpose of this study is to use an idealized cloud model to examine the structural changes that occur within an organized convective system as it interacts with a simplified city and to determine if systemically altering characteristics of the city (surface roughness length, urban surface temperature) yields predictable structural changes.

2. Experiments

Version 18 of the First-Generation Pennsylvania State University-National Center for Atmospheric Research Cloud Model (CM1) [34] is used to conduct a suite of idealized two-dimensional simulations in which a squall line interacts with a simplified representation of an urban area. CM1 is a highly scalable, energy-conserving cloud model specifically designed for idealized simulations of deep convection. The model is configured with a 600 km horizontal domain and a model top of 19.75 km. Stretched grids are used in both the horizontal and vertical directions. The horizontal grid spacing is 250 m within the innermost 120 km of the domain and gradually increases to 1 km outside this region. The vertical grid has 80 total levels with 50 m spacing below 3 km and 500 m spacing above 8.75 km. The model time step is adaptive and automatically adjusts to maintain computational stability. In all simulations the model time step varies between 3–4 s with 8–10 acoustic time steps for each large time step. The lateral boundary conditions are open-radiative, the bottom boundary condition is semi-slip, and the top boundary condition is a rigid wall. A Rayleigh damper is applied above $z = 15$ km in order to dissipate energy and prevent reflections off the top boundary. The Thompson double-moment microphysics parameterization [35] is used to represent precipitation processes. Subgrid turbulence is represented using the turbulent kinetic energy (TKE) based parameterization and the NASA Goddard parameterization is used for radiative processes.

All simulations utilize a horizontally homogenous base-state environment represented by the Weisman-Klemp analytic thermodynamic profile [28] combined with a unidirectional vertical wind profile from Rotunno et al. [30]. A vertical wind shear of 17.5 m s^{-1} is confined to the lowest 2.5 km. Convection is initiated at 150 km from the leftmost domain boundary using a thermal bubble. The thermal bubble has a radius of 10 km, is centered at 1.4 km above the surface, and has a maximum potential temperature perturbation of 1 K. The control simulation has a surface skin temperature of 300 K and surface characteristics (albedo, emissivity, and roughness length) of an herbaceous area. The surface roughness length (z_0) is set to 0.2 m. In the comparison simulations, a 20-km long region is inserted in the center of the domain to represent the idealized city. The skin temperature inside this region is enhanced to produce a feature comparable to an urban heat island. Surface roughness length is also increased to a value representative of a large urban area. Skin temperature is increased to values of 303, 305, and 307 K—producing differences relative to the area outside the city of 3, 5, and 7 K, respectively. To produce a range of horizontal z_0 gradients, values over the idealized city are

increased to 0.5, 1.0, 1.5, and 2 m, respectively. Table 1 shows the values tested within the parameter space. Simulations will be referred to by the magnitude of the difference in skin temperature between the idealized city and outlying area (ΔT) as well as the z_0 value of the city in the center of the domain. For example, “5Kz2.0” represents the simulation in which skin temperature within the city is 5 K larger than the surrounding area and the roughness length of the city is set to 2 m.

Table 1. Summary of the experiments within the parameter space. All experiments are identical except for two parameters: The surface roughness length (z_0) within the idealized city and the skin temperature perturbation (relative to the surrounding area) within the city (ΔT).

		Surface Roughness Length Over City (z_0)				
		0.2 m	0.5 m	1.0 m	1.5 m	2.0 m
Skin temperature perturbation over city (ΔT)	0 K	$\Delta T = 0, z_0 = 0.2$	$\Delta T = 0, z_0 = 0.5$	$\Delta T = 0, z_0 = 1.0$	$\Delta T = 0, z_0 = 1.5$	$\Delta T = 0, z_0 = 2.0$
	3 K	$\Delta T = 3, z_0 = 0.2$	$\Delta T = 3, z_0 = 0.5$	$\Delta T = 3, z_0 = 1.0$	$\Delta T = 3, z_0 = 1.5$	$\Delta T = 3, z_0 = 2.0$
	5 K	$\Delta T = 5, z_0 = 0.2$	$\Delta T = 5, z_0 = 0.5$	$\Delta T = 5, z_0 = 1.0$	$\Delta T = 5, z_0 = 1.5$	$\Delta T = 5, z_0 = 2.0$
	7 K	$\Delta T = 7, z_0 = 0.2$	$\Delta T = 7, z_0 = 0.5$	$\Delta T = 7, z_0 = 1.0$	$\Delta T = 7, z_0 = 1.5$	$\Delta T = 7, z_0 = 2.0$

Trajectory Analysis

In each simulation, 400,000 passive tracers are released into the flow at the beginning of the simulation. These tracers are advected at the model timestep using a 5th order Runge-Kutta advection scheme. The initial location of all tracers is confined between 200 and 600 km in the horizontal domain and between 0.025 and 1.475 km above the surface. Tracers within the storm updraft at a specific analysis time are followed backwards in time to determine their previous positions with a temporal resolution of 1 min. Model-calculated fields (e.g., buoyancy, vertical velocity) are interpolated to the tracer positions, also with a temporal resolution of 1 min.

3. Results

All simulations produce a squall line that develops from the initial thermal perturbation and travels left-to-right across the domain. By $t = 120$ min, the squall line has not yet passed over the idealized city in any of the simulations, but differences in the low-level thermodynamic structure over the idealized cities are readily apparent (Figure 1). In the control simulation (0Kz0.2), temperature is horizontally homogeneous in the environment ahead of the squall line. The same is true in all $\Delta T = 0$ K simulations. However, as ΔT increases, a dome-like structure in the near-surface temperature develops (see 3Kz0.2, 5Kz0.2, 7Kz0.2 simulations in Figure 1). As expected, the magnitude of the temperature excess in this thermal dome increases as ΔT is increased. Additionally, in simulations with $\Delta T > 0$ K, increasing z_0 results in a stronger and deeper thermal dome. For example, in the 7Kz0.2 simulation, the thermal dome structure does not extend above $z = 0.5$ km and temperature values within the dome are approximately 1 K warmer than areas outside the dome. In the 7Kz2.0 simulation, the thermal perturbation at the center of the domain extends up to 0.75 km and temperature values are 3–4 K larger than outside the dome. The depth of this dome is confined below $z = 1$ km in all simulations, in agreement with observations of real urban heat islands [36]. A further investigation (not shown) revealed that the simulations with enhanced z_0 produced larger eddy mixing coefficients, which more efficiently mixed the warmer temperatures from the heated surface.

Figure 2 shows the vertical structure of potential temperature (θ) at $t = 120$ min. In the control simulation (0Kz0.2), a low-level stratification is evident with θ decreasing with height across the domain. This same structure is also present in the other 0 K simulations as z_0 is increased over the city (0Kz0.5, 0Kz1.0, 0Kz1.5, 0Kz2.0). The introduction of a heated surface disrupts this stratification directly over the idealized city, leading to instances of constant θ with height in the lowest kilometer above the surface (3Kz0.2, 5Kz0.2, 7Kz0.2). This feature agrees with observations of real urban heat islands [37] although the depth of the neutral stratification varies across the parameter space simulations. As previously discussed, vertical mixing is enhanced when z_0 is increased. In the simulations with enhanced ΔT ,

increasing the z_0 gradient results in a deeper layer with near neutral θ stratification. For a given ΔT , the deepest heat islands are found with the largest z_0 values.

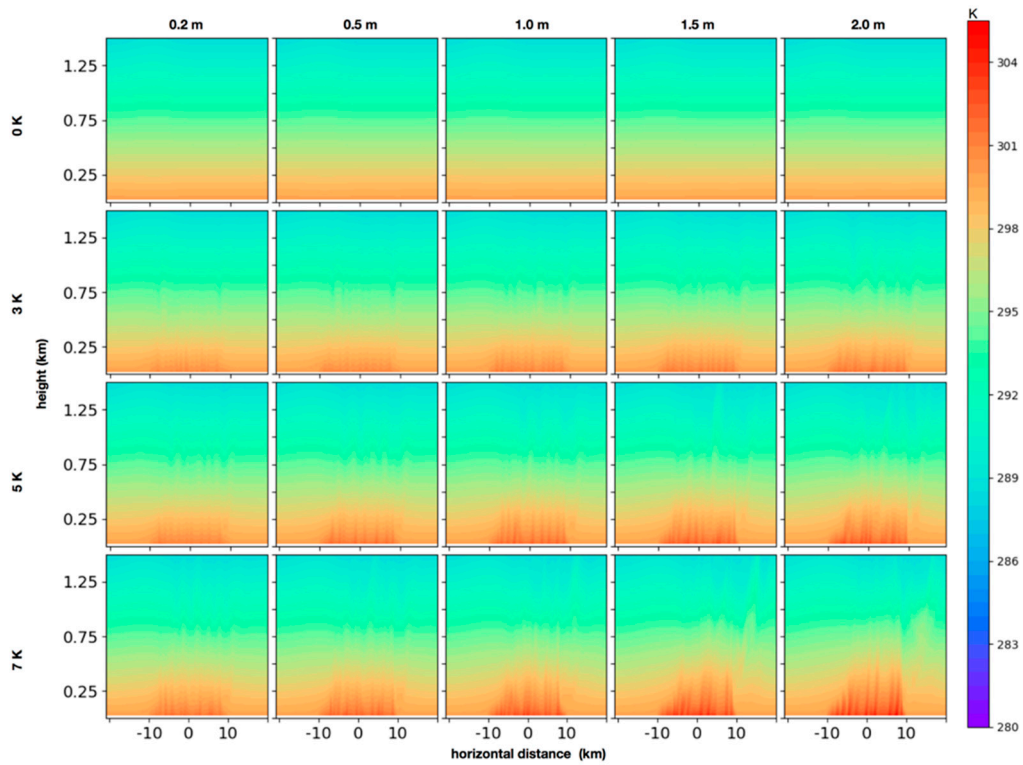


Figure 1. Cross-section of temperature (K) at $t = 120$ min. Each row represents simulations with a particular skin temperature perturbation within the idealized city while each column represents simulations with a particular z_0 value within the city.

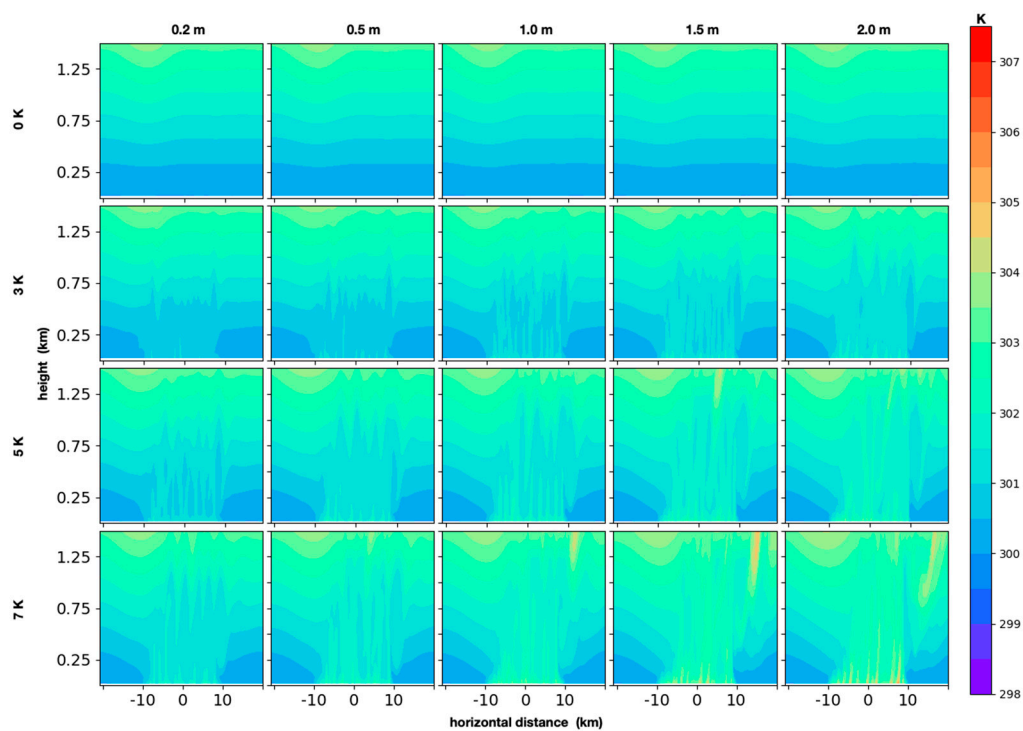


Figure 2. Same as Figure 1, except showing potential temperature (K).

The alterations to the low-level thermodynamic structure within the city have a dramatic impact on instability. Table 2 shows values of surface-based convective available potential energy (CAPE) and convective inhibition (CIN) averaged across the idealized city at $t = 120$ min. In the control environment, CAPE is 1932 J kg^{-1} and CIN is -46 J kg^{-1} . Increasing z_0 without increasing ΔT (top row in Table 2) results in a small CAPE increase and a negligible change in CIN. A much more noticeable change occurs when $\Delta T > 0 \text{ K}$. For a given value of z_0 , increasing ΔT results in a substantial increase in CAPE and a reduction in CIN (see the 3Kz0.2, 5Kz0.5, and 7Kz0.2 simulations). When $\Delta T > 0 \text{ K}$, increasing the z_0 gradient also results in increased CAPE and decreased CIN (see the 7Kz0.5, 7Kz1.0, 7Kz1.5, and 7Kz2.0 simulations). When comparing the control (0Kz0.2) and 7Kz2.0 simulations, CAPE increases from 1932 to 2855 J kg^{-1} (47% increase) while CIN decreases from -46 to -1 J kg^{-1} .

Table 2. Surface-based CAPE (J kg^{-1}) and CIN (J kg^{-1} , italicized) over the idealized city at $t = 120$ min.

		z_0				
		0.2 m	0.5 m	1 m	1.5 m	2 m
ΔT	0 K	1932 (-46)	1936 (-45)	1971 (-44)	1949 (-44)	1941 (-44)
	3 K	2056 (-25)	2055 (-21)	2198 (-14)	2226 (-11)	2290 (-8)
	5 K	2165 (-15)	2311 (-7)	2371 (-5)	2504 (-2)	2595 (-2)
	7 K	2289 (-7)	2409 (-4)	2616 (-1)	2784 (-1)	2855 (-1)

Variations in CAPE and CIN between simulations should be associated with changes to updraft intensity as storms approach and pass over the city. While this is true in the simulations, the relationship is not monotonic. In other words, the simulations with largest CAPE/lowest CIN do not necessarily yield the strongest updrafts. Table 3 shows the maximum instantaneous updraft velocity during a 60 min window ($t = 140$ min to $t = 200$ min) focused on the time period when the squall line passes over the idealized city. In the control simulation (0Kz0.2), the domain maximum vertical velocity is 41 m s^{-1} —the smallest value within the parameter space. When $\Delta T = 0 \text{ K}$, inducing a horizontal z_0 gradient results in larger values of maximum vertical velocity. Increasing ΔT while the horizontal z_0 gradient is zero or relatively modest ($z_0 = 0.2 \text{ m}, 0.5 \text{ m}$) also results in larger vertical velocities. The largest vertical velocities are found in the 5Kz0.5 and 7Kz0.5 simulations. Conversely, increasing ΔT in the simulations with larger z_0 gradients ($z_0 = 1.5 \text{ m}, 2.0 \text{ m}$) typically results in a much smaller increase relative to the control. Aside from the control simulation, the smallest instantaneous vertical velocities are found with large z_0 and large ΔT (e.g., the 5Kz2, 7Kz1.0, 7Kz1.5, and 7Kz2.0 simulations). While these simulations have the largest CAPE over the city, they also have the least amount of CIN. In these simulations, convection is initiated downwind of the city and interacts with the main squall line. This interaction may have negative consequences to storm intensity.

Table 3. Domain maximum vertical velocity (m s^{-1}) in each simulation over the period of $t = 140$ min to $t = 200$ min. This time period is centered on when the storms pass over the idealized city.

		z_0				
		0.2 m	0.5 m	1 m	1.5 m	2 m
ΔT	0 K	40.9	46.7	48.5	45.8	48.5
	3 K	42.9	43.7	46.5	44.5	44.9
	5 K	41.8	52.6	45.6	48.1	43.6
	7 K	48.7	53.2	42.4	42.1	41.7

Figure 3 shows the time-series of domain maximum vertical velocity over the duration of each simulation. During the first 80 min, all simulations produce an identical evolution with smaller differences emerging after this time. Each simulation exhibits a sharp ramp-up period over the first 50 min of simulation followed by a quasi-steady period that lasts until approximately $t = 120$ min. From $t = 120$ min through $t = 180$ min, most simulations exhibit a steady increase in maximum vertical velocity to a new quasi-steady state of roughly $35\text{--}40\text{ m s}^{-1}$. After $t = 200$ min, most of the simulations show a gradual weakening in the maximum updraft. Despite the overall similarities, differences in evolution are evident. For example, the 0Kz0.2 simulation exhibits updraft weakening between $t = 180$ min and $t = 210$ min followed by a restrengthening. In simulations with $\Delta T = 0\text{ K}$ and enhanced z_0 , the weakening is not present and the maximum vertical velocity is enhanced. For a given value of z_0 , an increase in ΔT does not appear to have a notable impact on the domain maximum vertical velocity in most simulations. The exception to this trend is the $z_0 = 0.5\text{ m}$ experiments. The 5Kz0.5 and 7Kz0.5 cases have an abrupt spike in maximum vertical velocity centered on the time of interaction with the idealized city that is not present in the 0Kz0.5 simulation. The 3Kz0.5 simulation does exhibit a spike in vertical velocity, however it occurs approximately 20–30 min after interaction with the city.

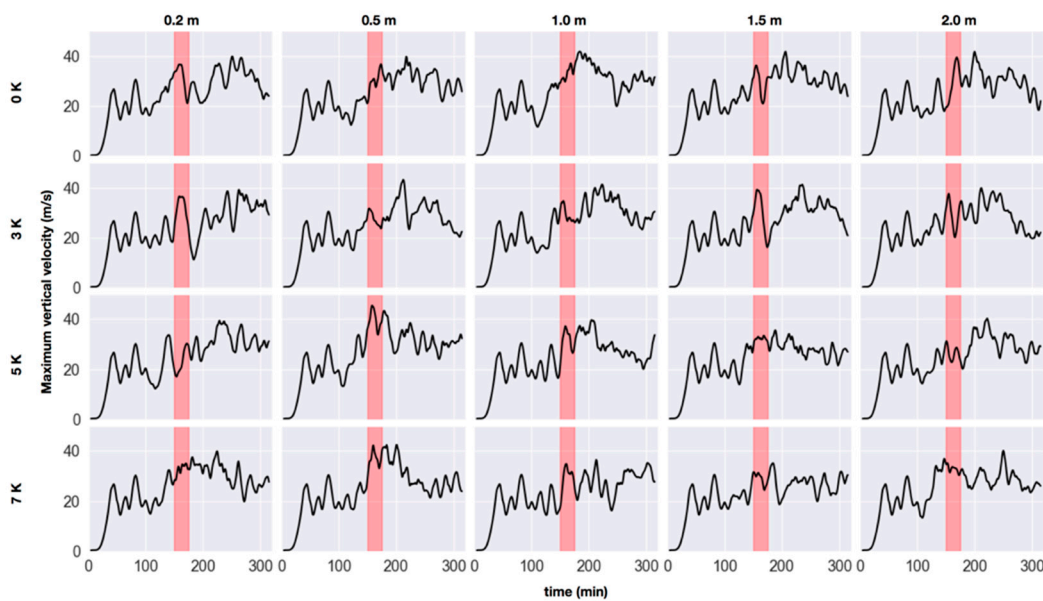


Figure 3. Domain maximum vertical velocity in each simulation. Values are smoothed using a 10-point moving filter using data with a 1-min temporal resolution. The red rectangle highlights the time period when the storm is passing over the idealized city.

More distinct changes in the updraft structure are evident when evaluating the total kinetic energy of upward motion within the domain. A term herein referred to as updraft kinetic energy (UKE) is defined as:

$$UKE = \sum_{i=1}^n \frac{1}{2} m_i w_i^2 \tag{1}$$

where m_i is the mass within the i th grid cell and w_i is the vertical velocity within the i th cell. The summation is over all points where $w > 1\text{ m s}^{-1}$ and within the cloud (total hydrometeor mixing ratio $> 1\text{ g kg}^{-1}$). The time-series of UKE for all simulations are shown in Figure 4. In the control simulation (0Kz0.2), UKE fluctuates below $2 \times 10^6\text{ J}$ until approximately $t = 200$ min when it increases to a maximum of over $4 \times 10^6\text{ J}$ between 250–300 min. When the z_0 gradient is increased and $\Delta T = 0\text{ K}$, the UKE maximum occurs earlier in time. For example, in the 0Kz2 simulation, UKE exceeds $4 \times 10^6\text{ J}$ before $t = 200$ min, approximately 60 min earlier than in the control simulation. When ΔT is increased but z_0 remains the same as the surroundings (e.g., 3Kz0.2, 5Kz0.2, 7Kz0.2), a similar trend is seen, with

the maximum at the end of the simulation moving to progressively earlier times. Other differences in the UKE evolution are also evident, but they do not exhibit a consistent trend. In the 3Kz0.2 simulation, there is a sharp increase in UKE to over 3×10^6 J during interaction with the idealized city. When ΔT is increased further (5Kz0.2, 7Kz0.2), that increase is no longer present. In simulations where both z_0 and ΔT are increased, a substantial increase in UKE often (but not always) occurs during or shortly after the city-storm interaction period (see the 3Kz0.5, 3Kz2.0, 5Kz0.5, 5Kz1.0, 5Kz1.5, 7Kz0.5, and 7Kz1.0 simulations). The largest increase is seen in the 5Kz0.5 simulation. In other simulations (3Kz1.5, 7Kz1.5, 7Kz2.0), no such increase is apparent.



Figure 4. Time series of the updraft kinetic energy (UKE) for each simulation. The red rectangle highlights the time period when the storm is passing over the idealized city.

Figure 5 shows the spatial structure of updrafts in each simulation at $t = 130$ min, approximately 15 min before the storm passes over the idealized city in the center of the domain. In all simulations, the main updraft is 30–40 km to the left of the domain center. The maximum vertical velocity is approximately 20 m s^{-1} in all simulations except 0Kz0.5 (13 m s^{-1}). Additionally, the cloud top height is approximately 11–12 km in all simulations. Development of new convection is evident downwind of the idealized city in the simulations with large ΔT and large z_0 (5Kz1.0, 5Kz2.0, 7Kz1.0, 7Kz1.5, 7Kz2.0). The location of the new development is the same in each of these simulations—approximately 20 km to the right of the city center—but the updraft strength in these new cells increases as ΔT and z_0 are increased.

Figure 6 shows the vertical velocity structure 40 min later, after the storms have passed over the idealized city. In most simulations, the primary updraft is stronger and extends to a higher altitude relative to the structure at $t = 130$ min. In addition to stronger updrafts, the cloud area has also expanded in all cases. In the cases with large ΔT and large z_0 gradients (e.g., 5Kz2.0, 7Kz1.0, 7Kz1.5, 7Kz2.0), the convection on the downwind side of the city has become more expansive compared to the earlier time, with cells extending up to 70 km downwind of the city center. In the absence of a heat island ($\Delta T = 0 \text{ K}$), increasing the horizontal z_0 gradient results in stronger updrafts. Compared to the control simulation, the 0Kz0.5, 0Kz1.0, and 0Kz2.0 have stronger updrafts at $t = 170$ min. In the

$z_0 = 0.2$ m simulations, increasing ΔT also results in stronger and deeper updrafts. When compared to the control simulation, the 3Kz0.2, 5Kz0.2, and 7Kz0.2 simulations all have stronger updrafts, particularly between 5 and 10 km above the surface. When both ΔT and the z_0 gradient are increased, most simulations contain updrafts that are stronger and deeper compared to the control simulation, however systematically increasing one parameter (either ΔT or z_0) does not always lead to stronger updrafts. For example, the updraft in the 3Kz0.2 simulation appears stronger than in the 3Kz0.5 or 3Kz2.0 simulations. The strongest updrafts at $t = 170$ min occur in the 0Kz2.0, 5Kz0.5, 5Kz1.0, and 7Kz1.0 simulations.

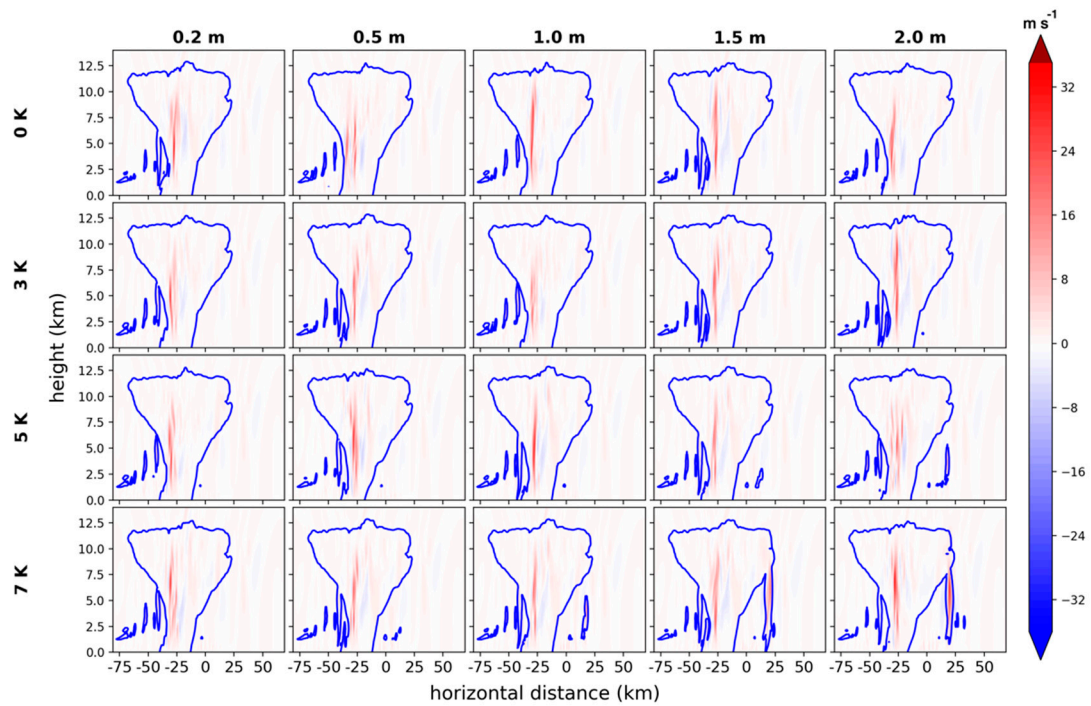


Figure 5. Vertical velocity (colored) at $t = 130$ min in each simulation. The blue contour represents a hydrometeor mixing ratio of 0.02 g kg^{-1} .

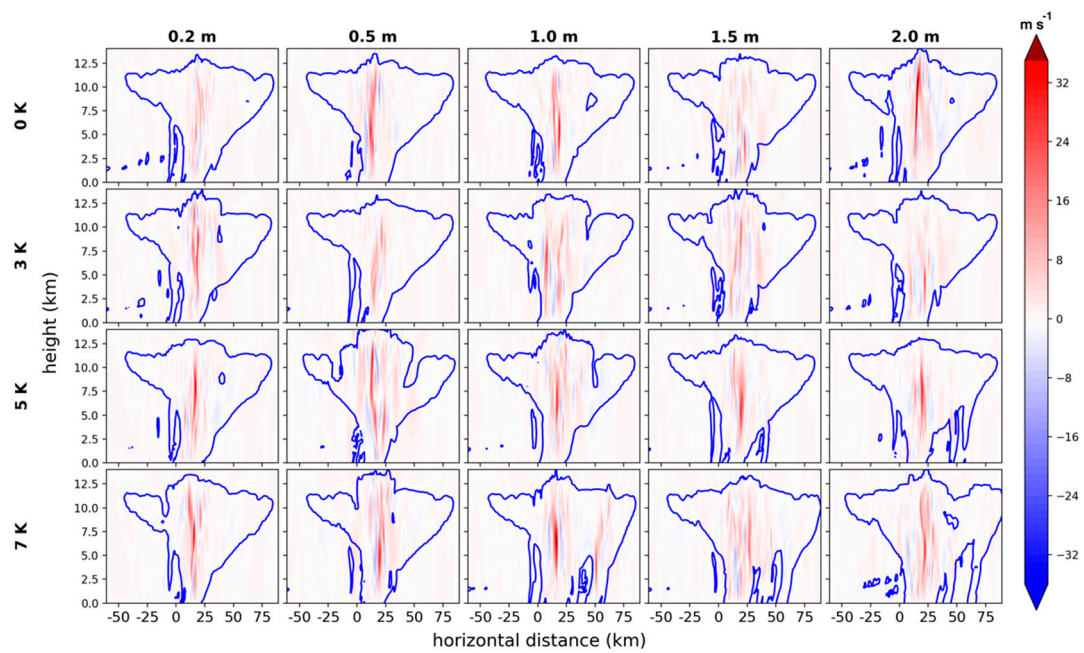


Figure 6. Same as Figure 5, except at 170 min.

Changes in the vertical velocity before and after interaction with the idealized city are further emphasized in Figure 7. Changes to the updraft intensity and/or size are smallest in magnitude in the control simulation (0Kz0.2). As the surface z_0 gradient is increased (top row of Figure 7), a more noticeable updraft strengthening is apparent. When ΔT is increased but the z_0 gradient remains zero (0Kz0.2, 3Kz0.2, 5Kz0.2, and 7Kz0.2 simulations), updraft strengthening is evident at mid to upper levels. When both ΔT and the surface z_0 gradient are enhanced, changes to the updraft structure range from minimal (e.g., 3Kz0.5) to expansive (e.g., 5Kz0.5).

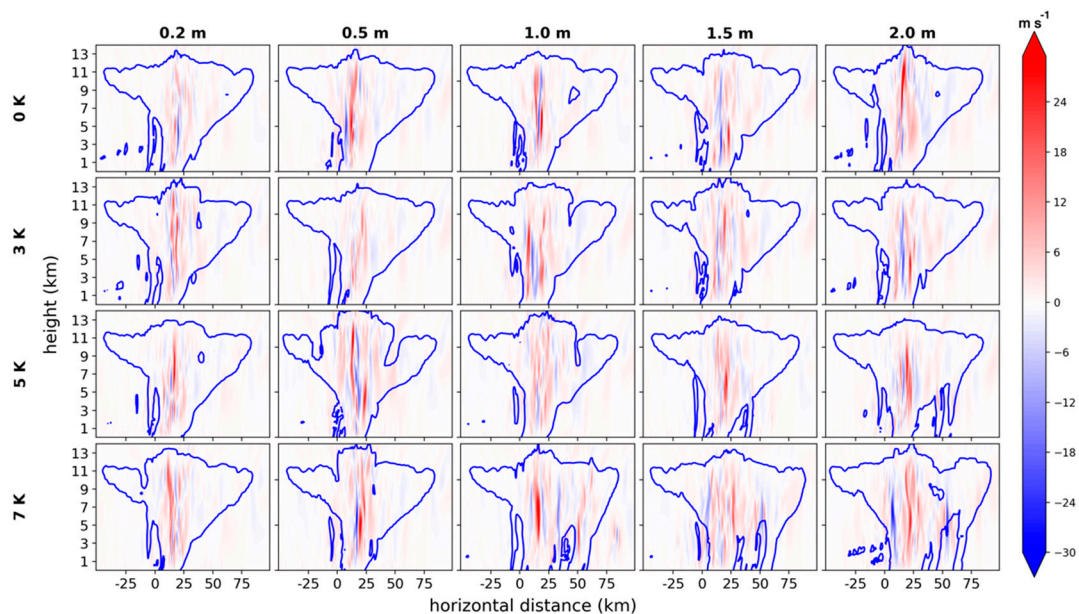


Figure 7. Change in vertical velocity between $t = 130$ min and $t = 170$ min (colored) in each simulation. The blue contour represents the hydrometeor mixing ratio of 0.02 g kg^{-1} at $t=170$ min. The colored field was calculated by subtracting the vertical velocity field at $t = 170$ min from the same field at $t = 130$ min after adjusting for a storm motion in the earlier field using the mean environmental winds.

Variability in vertical velocity between simulations is associated with changes to low-level divergence. Figure 8 shows divergence and vertical velocity at $t = 145$ min in all simulations. The impact of horizontal z_0 gradients is most evident in the $\Delta T = 0$ K simulations (top row of Figure 8). For example, in the 0Kz0.2 simulation there is a small area of divergence centered on the location of the idealized city ($x = 0$ km). As the z_0 gradient is increased, convergence increases in both magnitude and area over the city. In the 0Kz2.0 simulation, convergence extends almost to the lateral edges of the city ($x = -10$ km to $x = 10$ km) and extends upward beyond 2 km above the surface. This area of convergence is associated with updrafts directly over the city above $z = 1$ km. While the simulations with $\Delta T > 0$ K have somewhat chaotic patterns in convergence/divergence (rows 2–4 in Figure 8), there are coherent patterns in relation to vertical velocity. Increasing ΔT results in areas of updraft extending closer to the surface (see the 0Kz0.2, 3Kz0.2, and 5Kz0.2 simulations). In general, low-level divergence is associated with downdrafts while areas of low-level convergence are associated with updrafts.

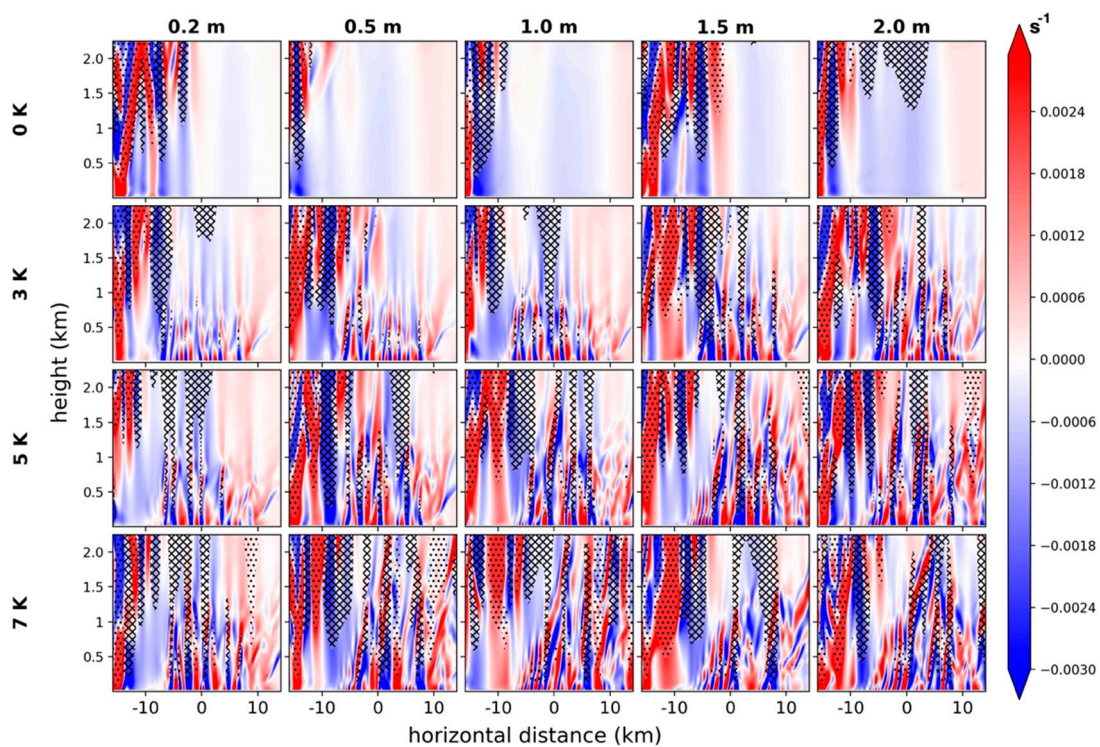


Figure 8. Divergence (colored) and vertical velocity (hatched contours are areas greater than 1 m s^{-1} and stippled areas are areas less than -1 m s^{-1}) at $t = 145$ min. Negative values indicate convergence.

Low-level divergence patterns in three of the $\Delta T = 0$ K simulations (0Kz0.2, 0Kz1.0, and 0Kz2.0) at $t = 145$ min are shown in Figure 9. At this time, the leading edge of the squall line is interacting with the leftmost edge of the idealized city ($x = -10$ km). As the storm approaches, outflow from the negative- x direction is directed over the city. On the opposite side of the city, low-level inflow approaches the leading edge of the storm from the positive- x direction. At the interface of the inflow and outflow, convergence is present. In the 0Kz0.2 simulation, the near-surface convergence is fairly weak and there is a small area of divergence directly over the idealized city ($x = 0$ km). When the surface z_0 gradient is increased, the inflow into the storm is slowed over the idealized city, resulting in a broader and stronger area of near-surface convergence in the 0Kz1.0 and 0Kz2.0 simulations.

Updraft strengthening is also associated with changes in buoyant accelerations. Buoyancy (B) is calculated as $B = g \frac{\theta_p - \theta_{p0}}{\theta_{p0}}$, where g is gravitational acceleration, θ_p is density potential temperature, and subscript 0 indicates the base-state value. Buoyancy values along forward-integrated parcel trajectories are analyzed and traced backwards for 50 min. Trajectories are filtered based on a vertical velocity threshold at the defined analysis time. For example, Figure 10 only shows the location history of

parcels with a vertical velocity greater than 1 m s^{-1} at $t = 120 \text{ min}$. These parcels are traced backwards for 50 min to determine their origin location and buoyancy history. In all simulations, the majority of parcels originate ahead of the storm, although some parcels do appear to originate in the storm outflow. In all simulations, the updraft parcels exhibit a midlevel maximum in B between 4 and 10 km above the surface. The magnitude of the maximum B values is similar between simulations. The same is true for the spatial extent of the maximum. One of the more notable differences is seen near the surface. As ΔT and the z_0 gradient are increased, near surface B values also increase.

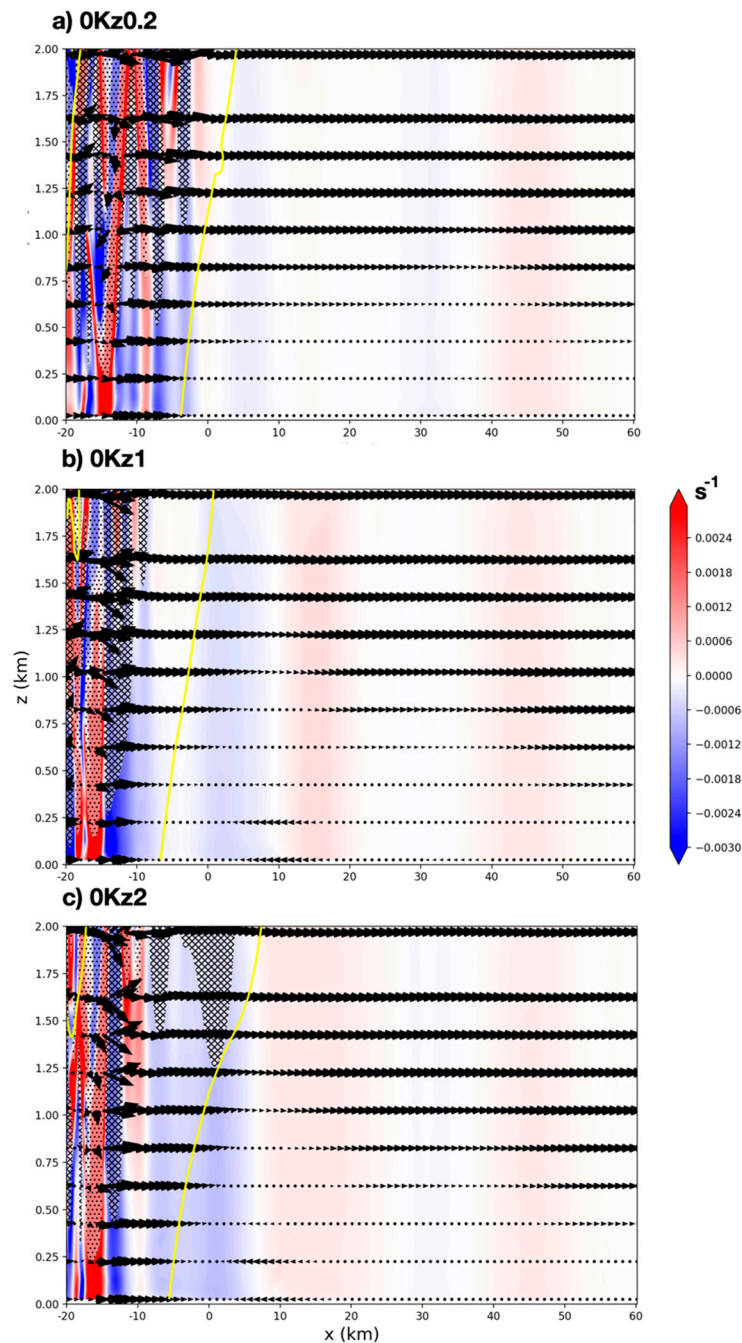


Figure 9. Divergence (colored), wind arrows, and vertical velocity (hatched areas are $> 1 \text{ m s}^{-1}$ and stippled areas are $< -1 \text{ m s}^{-1}$), at $t = 145 \text{ min}$ in three select simulations. The arrow length is proportional to wind speed. The yellow contour represents the hydrometeor mixing ratio value of 0.02 g kg^{-1} .

By $t = 165$ min (after passing over the idealized city) there are much more apparent differences between simulations (Figure 11). In all simulations, the overall area covered by the largest B values has increased both horizontally and vertically. For example, at $t = 120$ min (Figure 10) in the 3Kz0.2 simulation, B values greater than $1 \times 10^{-4} \text{ m s}^{-2}$ are concentrated mainly in a narrow horizontal area between 5 and 7.5 km above the surface. By $t = 165$ min (Figure 11), B values above this threshold are found below 4 and above 10 km. The horizontal extent also increased substantially. While all simulations show an increase in B between 120 and 165 min, the increase is greatest in the simulations with larger ΔT and larger z_0 gradients. The smallest differences in B are found in the 0Kz0.2, 0Kz0.5, 3Kz0.2, and 3Kz0.5 simulations. Updrafts within the cells initiated downwind of the idealized city experience substantial buoyant accelerations in the 7Kz1.0, 7Kz1.5, and 7Kz2.0 simulations.

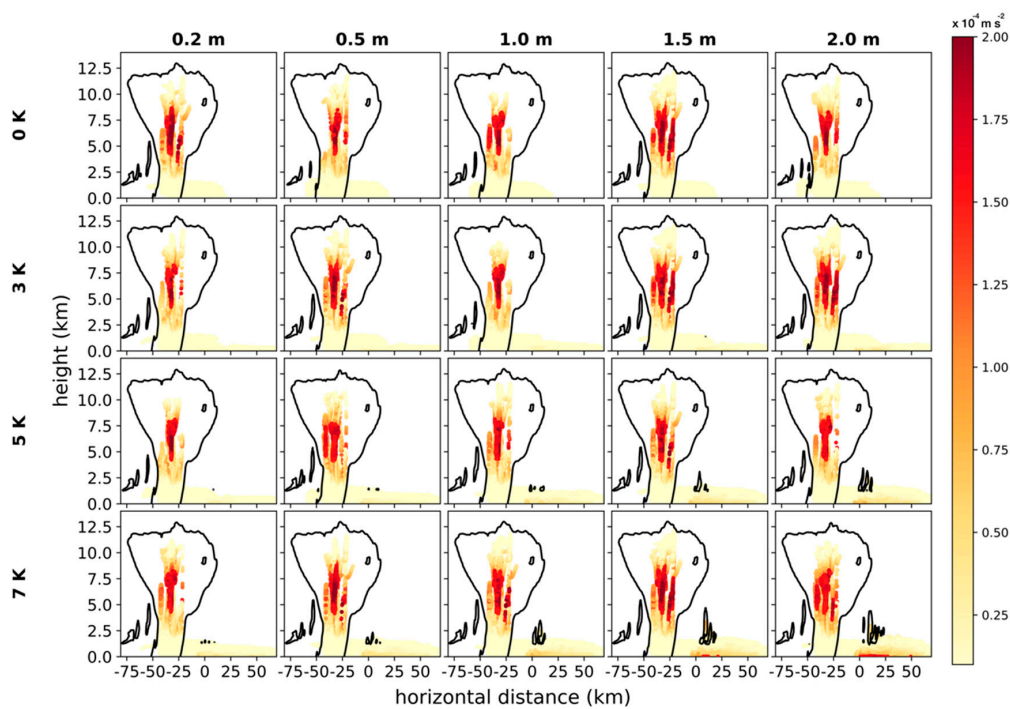


Figure 10. Time-space evolution of forward-integrated parcel trajectories that are located in the updraft at $t = 120$ min. The position of each parcel over the previous 50 min is shown, with a temporal resolution of 1 min. At each location, the parcel's location marker is colored by B. The black line is the 0.02 g kg^{-1} contour hydrometeor mixing ratio at $t = 120$ min.

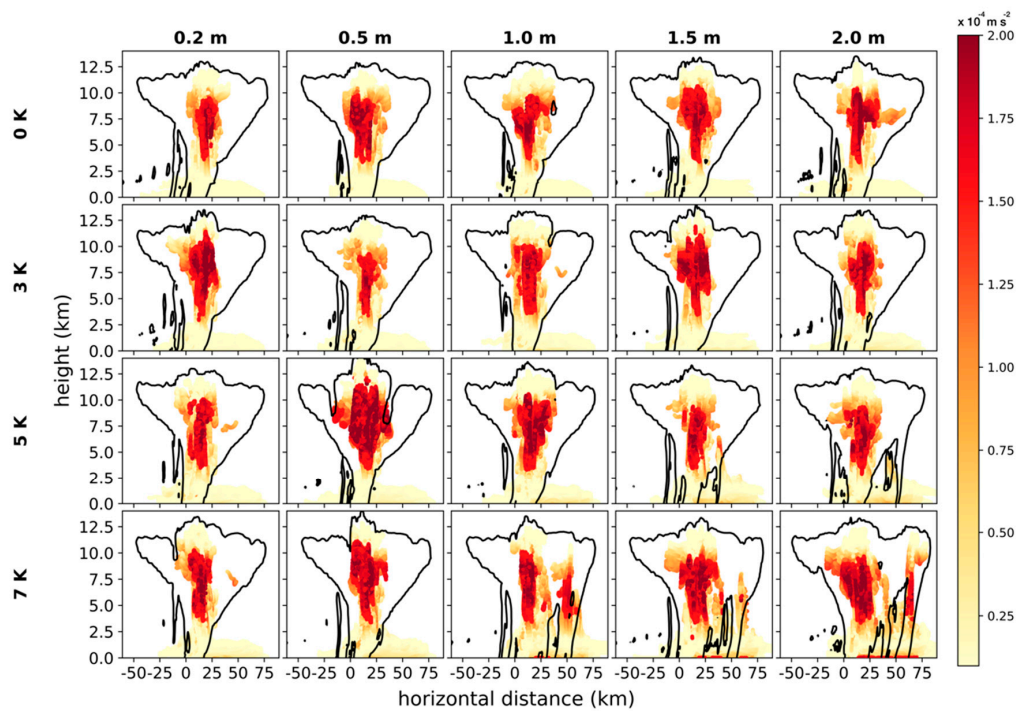


Figure 11. Same as Figure 10, except at $t = 165$ min.

Further insights into the temporal evolution of updraft accelerations can be gained by analyzing contoured frequency by altitude diagrams (CFADs; Yuter and Houze [38]) of B . Figure 12 shows CFADs of maximum B along parcel trajectories for all simulations at $t = 120$ min. At this time, CFADs of B are very similar. In all simulations, most parcels achieve maximum buoyancy below 8 km and all parcels achieve a maximum B less than $2.5 \times 10^{-4} \text{ m s}^{-2}$.

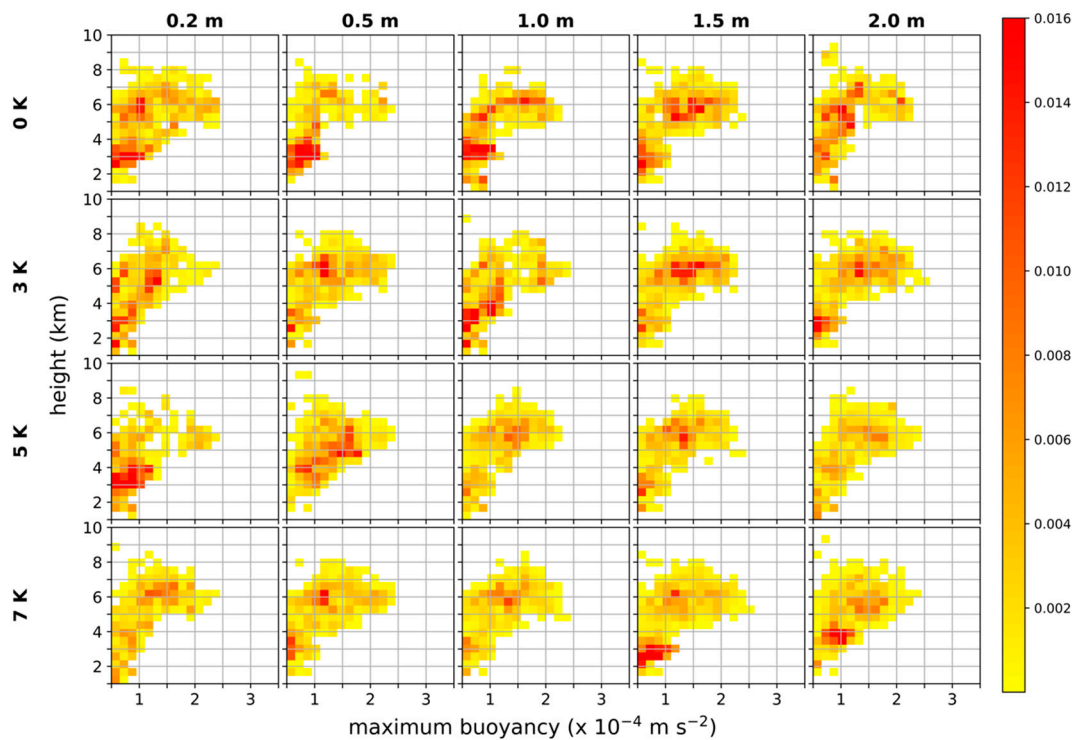


Figure 12. CFADs of maximum buoyancy along forward-integrated trajectory parcels located within an updraft at $t = 120$ min for each simulation. Maximum buoyancy is determined by examining the parcel's history over the previous 50 min. Only parcels that achieve positive buoyancy are shown.

Figure 13 shows CFADs of B at $t = 165$ min. In the control simulation (0Kz0.2), maximum B values are similar to those at $t = 120$ min (Figure 12). One difference at $t = 165$ min is that some parcels achieve maximum B above 8 km, but all maximum values of B in the control simulation remain less than $2.5 \times 10^{-4} \text{ m s}^{-2}$. In contrast, updrafts in simulations with larger ΔT and/or larger z_0 gradient vary from the control in several important ways. First, parcel trajectories that achieve a large positive B (greater than $2.0 \times 10^{-4} \text{ m s}^{-2}$) become more common compared to the earlier time and parcels achieve this large B over a more diverse range of heights. Second, the maximum B of any one parcel increases. In many of the simulations, some parcels achieve a maximum B greater than $3 \times 10^{-4} \text{ m s}^{-2}$.

The vertical perturbation pressure gradient force (vppgf) calculated along each parcel trajectory is shown in Figure 14. The parcels shown in Figure 14 are located in the updraft at $t = 165$ min and traced backwards for 50 min. All simulations contain a 'patch' of large values of vppgf at low levels. In most of the simulations, a narrow band of larger vppgf extends upwards in the main updraft. One of the larger differences between the simulations is seen near the cloud top, which is above 10 km. It can be seen that for a given ΔT , increasing the horizontal z_0 gradient typically results in a stronger vppgf near the cloud top. The increased vppgf near the cloud top indicates that these simulations contain wider updrafts, as shown in previous studies [39–41].

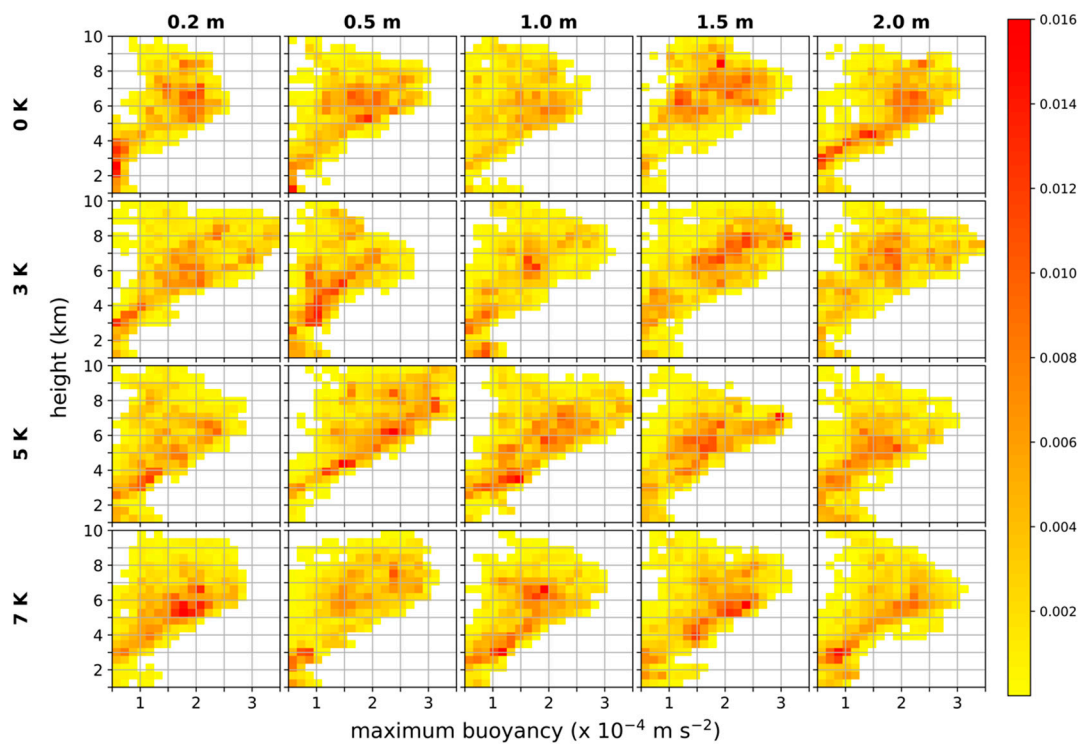


Figure 13. Same as Figure 12, except at $t = 165$ min.

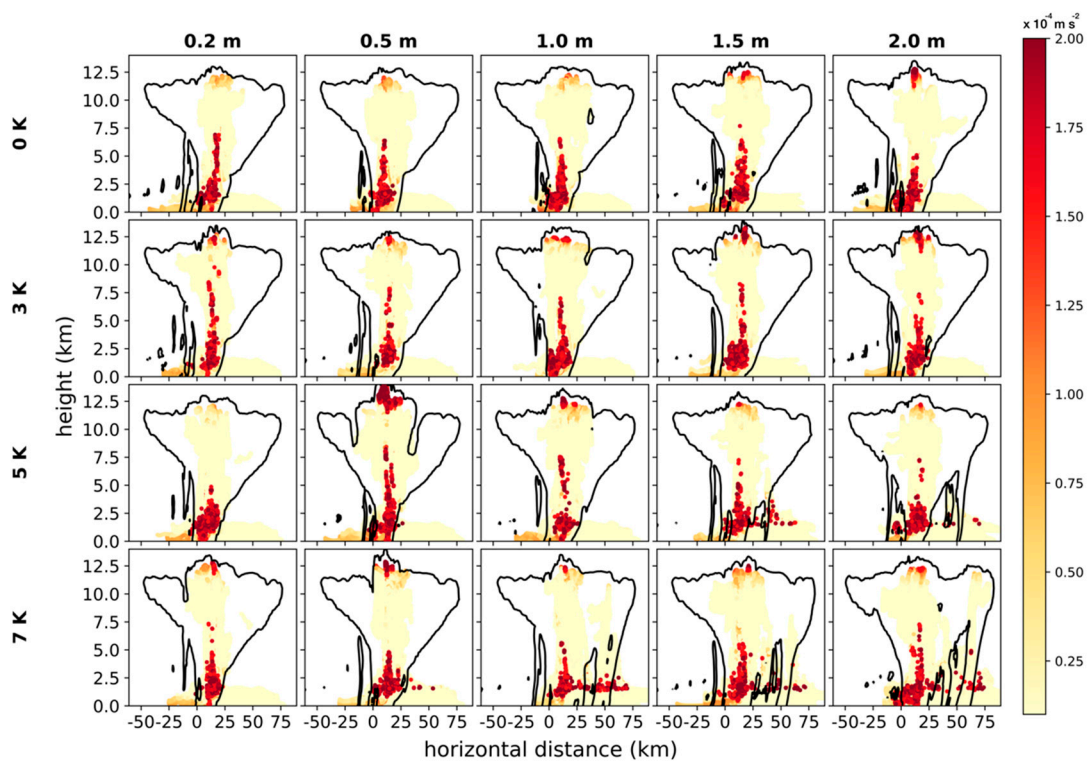


Figure 14. Same as Figure 11, except the parcel location is shaded by the vertical perturbation pressure gradient force.

Figure 15 displays an updraft mass flux (F_m), which is calculated as $F_m = \sum \max(w_{i,k}, 0) dx^2$, where $w_{i,k}$ is the vertical velocity at the i th horizontal and k th vertical grid point, and dx is the horizontal

grid spacing. At $t = 120$ min in the control simulation (0Kz0.2), F_m increases steadily from the surface until reaching a maximum value around 4 km above the surface at which point F_m decreases steadily until approximately 12 km above the surface. Above 12 km, F_m exhibits little change with height. At $t = 165$ min, the F_m profile in the control simulation is nearly identical to that at the earlier time. At both $t = 120$ min and $t = 165$ min, maximum F_m in the control simulation is approximately $2.2 \times 10^7 \text{ kg s}^{-1}$. The primary difference between the two times is a slight increase in F_m aloft beginning at approximately 7 km above the surface. In contrast, when $\Delta T = 0 \text{ K}$, increasing the horizontal z_0 gradient results in progressively larger F_m after interaction with the idealized city. The F_m maximum also tends to occur at a higher altitude as z_0 is increased. In the 0Kz2.0 simulation, the maximum F_m at $t = 165$ min increases to $3.0 \times 10^7 \text{ kg s}^{-1}$, which is an increase of over 36% compared to the control simulation. Increasing ΔT while holding the horizontal z_0 gradient to zero results in a similar trend. In the 3Kz0.2 simulation, the peak F_m value reaches $2.6 \times 10^7 \text{ kg s}^{-1}$ between 4 and 6 km above the surface while the 5Kz0.2 simulation has a maximum F_m of $2.9 \times 10^7 \text{ kg s}^{-1}$. Increasing ΔT further (7Kz0.2) results in a slightly smaller maximum F_m ($2.7 \times 10^7 \text{ kg s}^{-1}$). For a fixed value of ΔT (z_0), increasing z_0 (ΔT) typically results in increased F_m . The largest F_m value is seen in the 7Kz2.0 simulation, where the maximum of $3.7 \times 10^7 \text{ kg s}^{-1}$ is 68% larger compared to the maximum in the control simulation.

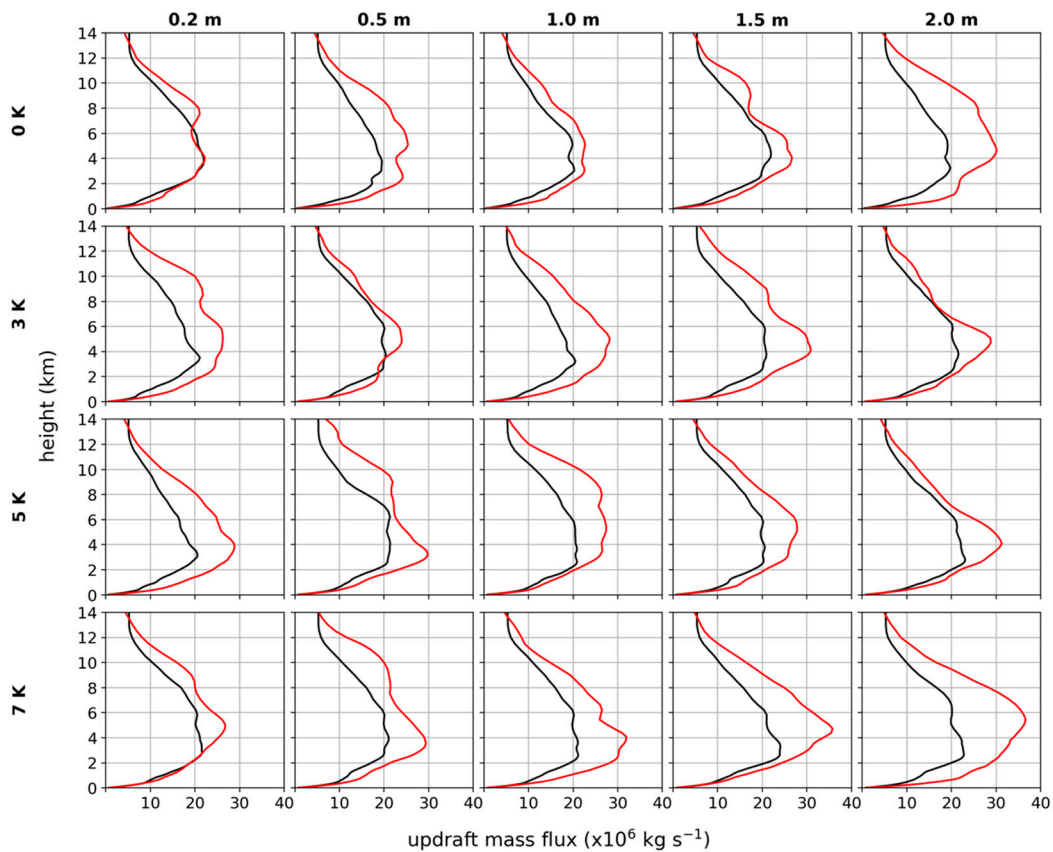


Figure 15. Updraft mass flux at $t = 120$ min (black line) and $t = 165$ min (red line).

Stronger, more vigorous updrafts may increase the likelihood of surface or near-surface convective hazards such as flash flooding, hail, or damaging winds. Figure 16 shows time series plots of domain total graupel/hail mass (m_{graup}) in each simulation. In the control simulation, there is a steady upward trend from $t = 100$ min through approximately $t = 170$ min, with a maximum value of $4.7 \times 10^7 \text{ kg}$. After the maximum is achieved, there is a slight reduction in m_{graup} before the values become steady. Within the tested parameter space, the control contains the smallest maximum m_{graup} value during the 100 to 200 min time window. When the horizontal z_0 gradient is increased but ΔT remains zero,

a substantial increase in m_{graup} (relative to the control simulation) occurs. In the 0Kz0.5 simulation, m_{graup} surpasses the maximum in the control simulation before the squall line passes over the city. By $t = 170$ min, after the storm has passed over the city, m_{graup} exceeds 8×10^7 kg. In the 0Kz2.0 simulation, maximum m_{graup} exceeds 10×10^7 kg at $t = 200$ min. Increasing ΔT while $z_0 = 0.2$ m results in similar increases to m_{graup} . In the 3Kz0.2 simulation, the time evolution of m_{graup} is similar to the control simulation except that the peak is greater— 5.8×10^7 kg compared to 4.7×10^7 kg. In addition, during interaction with the idealized city the rate of increase (inferred from the slope of the time-series line) is substantially greater in the 3Kz0.2 simulation compared to the control. In the 7Kz0.2 simulation, the rate of increase is similar to the 3Kz0.2 simulation but the period of increase is longer and the peak in m_{graup} is also substantially larger. When both ΔT and the horizontal z_0 gradient are increased, many of the simulations exhibit a drastic increase in m_{graup} during (or slightly after) interaction with the city (see 3Kz1.5, 5Kz0.5, 5Kz1.0, 5Kz1.5, 7Kz0.5, 7Kz1.0, 7Kz1.5). An additional difference can be seen prior to interaction with the idealized city. In the control simulation, m_{graup} remains between 2×10^7 kg and 3×10^7 kg from $t = 100$ min through $t = 130$ min before steadily increasing. Many of the simulations with enhanced ΔT and/or z_0 exhibit a decrease in m_{graup} around this time, with several of the simulations exhibiting rather sharp decreases just prior to interacting with the idealized city (0Kz0.5, 3Kz0.2, 3Kz1.0, 5Kz0.2).

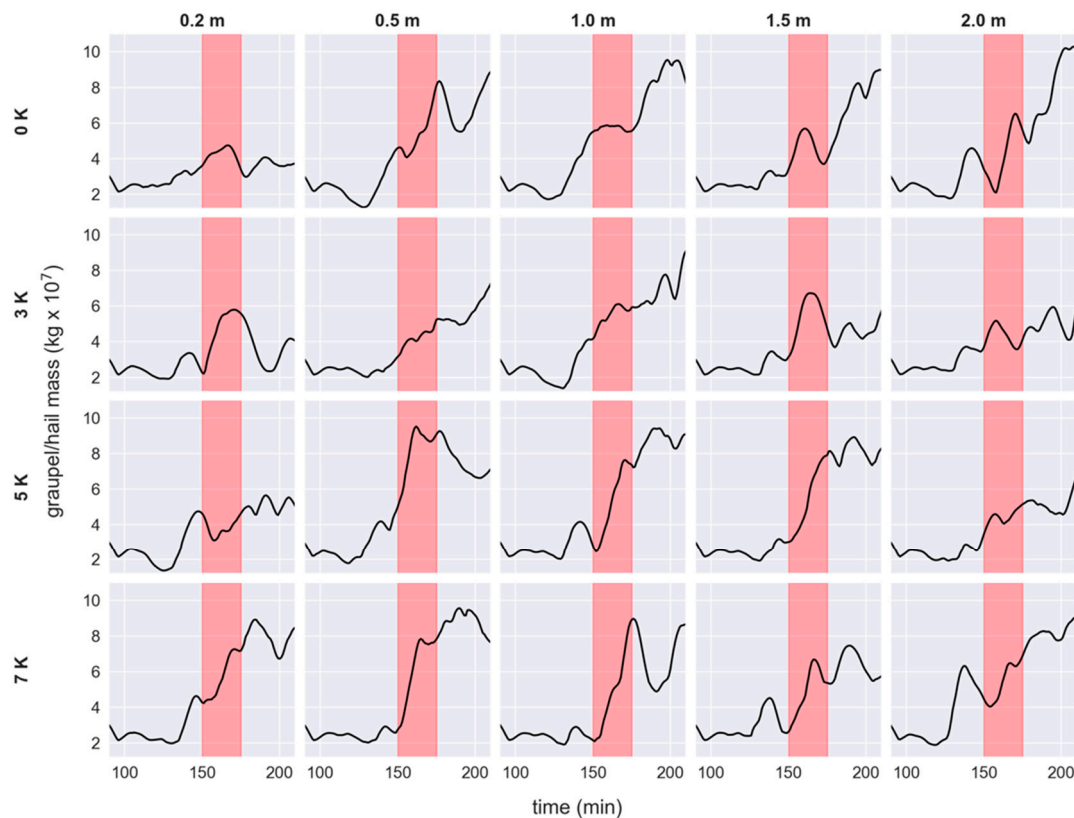


Figure 16. Time-series of domain total graupel/hail mass values. The red rectangle highlights the time period when the storm is passing over the idealized city.

A similar evolution is apparent in the domain total rain mass (m_{rain}). Figure 17 shows that in the control simulation, the m_{rain} is relatively constant from $t = 100$ min through $t = 200$ min, except for a slight increase in m_{rain} after $t = 180$ min which quickly subsides. In contrast, when ΔT remains zero, simulations with an enhanced z_0 gradient produce more substantial increases in m_{rain} following interaction with the city. Increasing ΔT also tends to result in larger m_{rain} . All of the $\Delta T = 7$ K simulations have a maximum m_{rain} of greater than 4.0×10^7 kg during the time window shown in Figure 17, whereas for the $\Delta T = 0$ K and $\Delta T = 3$ K simulations, only 0Kz1.0 and 3Kz1.0 contain m_{rain}

exceeding 4.0×10^7 kg. In addition, many of the simulations (0Kz2.0, 3Kz1.0, 3Kz1.5, 5Kz0.2, 5Kz0.5, 5Kz1.0, 5Kz2.0, 7Kz0.2, 7Kz1.0, 7K1.5, 7K2.0) exhibit a pronounced increase in m_{rain} when the squall line is passing over the idealized city.

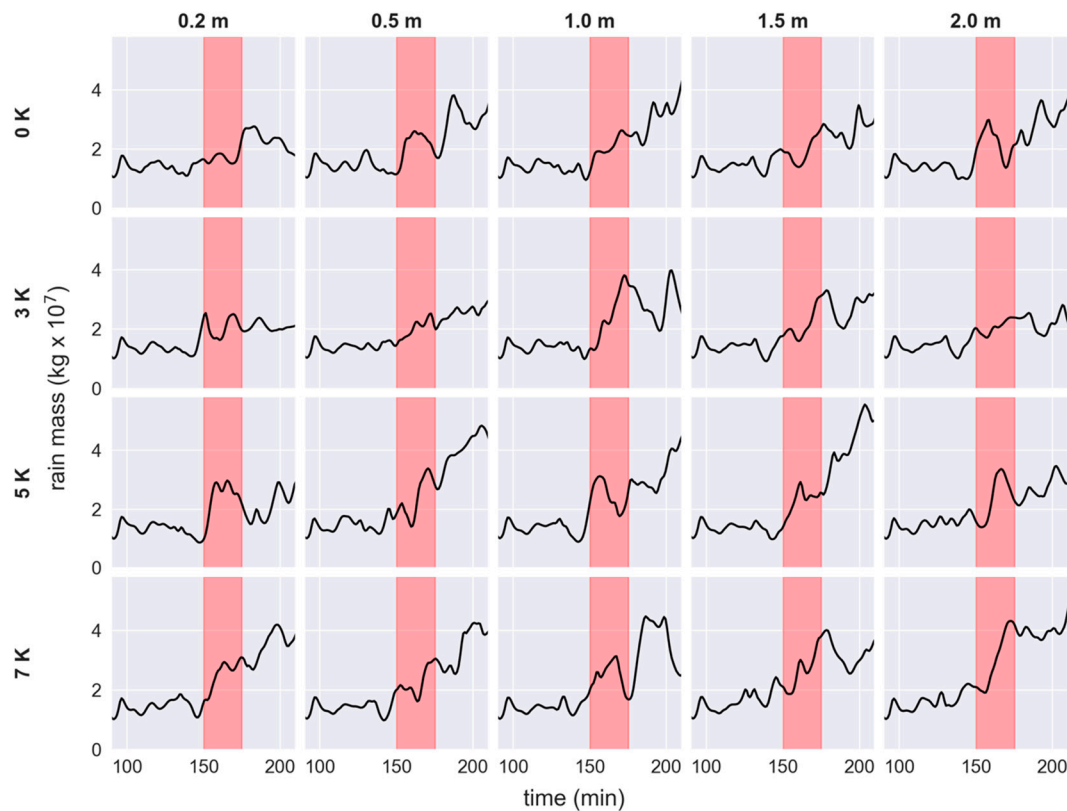


Figure 17. Same as Figure 16, except for rain mass.

While nearly every simulation with increased ΔT and/or z_0 produces larger m_{rain} relative to the control simulation, there is no predictable pattern in m_{rain} when either ΔT or z_0 is increased. For example, the 3Kz0.2 simulation does not show much of an increase in m_{rain} (relative to the control simulation) during or after interaction with the idealized city, whereas the 3Kz1.0 simulation contains a substantial increase in m_{rain} just prior to $t = 200$ min. However, further increasing the z_0 gradient (3Kz1.5) results in a smaller peak in m_{rain} , while the 3Kz2.0 does not contain a sharp peak at all. Increasing ΔT also yields inconsistent results. The 5Kz0.2 and 7Kz0.2 have similar increases in m_{rain} between $t = 180$ min and $t = 200$ min. The same is true for the 5Kz0.5 and 7Kz0.5 simulations.

Figure 18 shows cross-sections of the graupel/hail mixing ratio (q_g) after interaction with the idealized city. In the control simulation, the largest q_g values are found between 3 and 5 km above the surface, with a maximum value of 6.6 g kg^{-1} . Increasing z_0 over the city while $\Delta T = 0 \text{ K}$ results in larger values of q_g as well as an increase in the area of $q_g > 1 \text{ g kg}^{-1}$. Increased q_g is also found when ΔT is increased while z_0 remains 0.2 m. The largest values of q_g are found in the simulations where both ΔT and the horizontal z_0 gradient are increased. In particular, a maximum q_g in both the 5Kz1.0 and 7Kz0.5 simulations exceed 13 g kg^{-1} . Within the tested parameter space, only the 3Kz0.2 simulation yields a smaller maximum q_g value at $t = 190$ min compared to the control simulation.

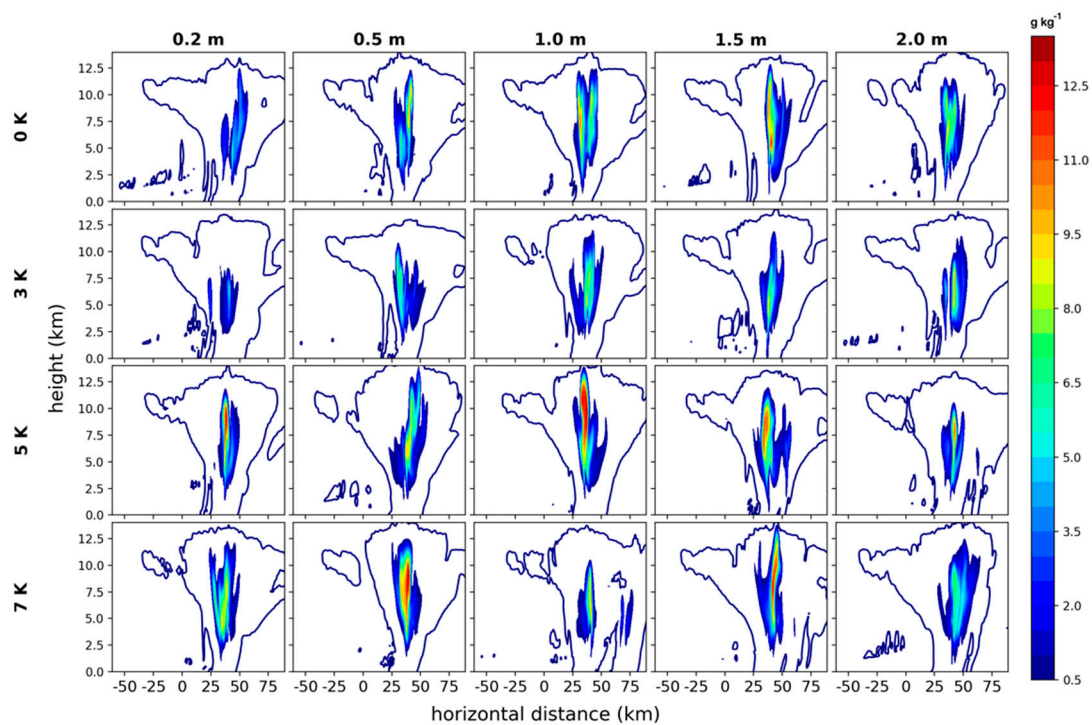


Figure 18. Vertical cross-sections of the graupel/hail mixing ratio at $t = 190$ min. The blue contour represents the hydrometeor mixing ratio of 0.02 g kg^{-1} .

Interaction with the idealized city also has an impact on the near-surface winds. Figure 19 shows the time-series of the maximum 10-m wind speed in each simulation. In the control simulation, the maximum fluctuates around 10 m s^{-1} between $t = 100$ min and $t = 170$ min. After 170 min, there is a sharp, brief increase to a peak value of 14 m s^{-1} followed by a slight decrease. This value (14 m s^{-1}) represents the smallest peak 10-m wind speed in any of the simulations. In the 0Kz0.5 simulation, the peak maximum is larger compared to the control simulation (24.5 m s^{-1} vs. 14 m s^{-1}) and occurs approximately 10 min earlier. While this peak value is short-lived, values of roughly 15 m s^{-1} persist until the end of the simulation (not shown). The remaining $\Delta T = 0 \text{ K}$ simulations also exhibit steady maximum winds of roughly 15 m s^{-1} after interaction with the city, although none have the drastic peak seen in the 0Kz0.5 simulation. Increasing ΔT also results in increased maximum values. For example, in the 3Kz0.2 simulation, the maximum wind speed of 16 m s^{-1} occurs 36 min prior to the maximum in the control simulation, when the squall line begins interacting with the idealized city. Further increasing ΔT to 5 K results in even stronger 10-m winds. A value of 16 m s^{-1} occurs during the interaction with the idealized city, and another peak of 21 m s^{-1} occurs around $t = 200$ min. In the 7Kz0.2 simulation, the maximum 10-m wind is larger than in the control and 3Kz0.2, but weaker than in 5Kz0.2. Many of the simulations with enhanced ΔT and horizontal z_0 gradients produce sharp peaks in the maximum 10-m wind during or shortly after interaction with the idealized city. The strongest winds are found in the 3Kz1.0 (23.6 m s^{-1} at 222 min), 3Kz2.0 (25 m s^{-1} at 203 min), 5Kz0.5 (25 m s^{-1} at 171 min), 5Kz1.0 (21 m s^{-1} at 200 min), 7Kz0.5 (23 m s^{-1} at 182 min), and 7Kz1.0 (24.5 m s^{-1} at 212 min).



Figure 19. Time-series of 10-m wind speed. The red rectangle highlights the time period when the storm is passing over the idealized city.

4. Discussion

Results indicate that increasing both the magnitude of ΔT and the horizontal gradient in z_0 leads to a deeper and stronger heat island. By many metrics (e.g., maximum updraft velocity, buoyant acceleration, updraft mass flux, graupel mass, 10-m winds), the squall line produced in the control simulation is weaker compared to simulations in which the squall line interacts with a well-defined idealized city. In many instances, increasing the heat island leads to a more substantial modification of the squall line as it passes over the city. However, increasing ΔT or the horizontal z_0 gradient by a defined increment does not always produce an increase in the response (for example, updraft intensity) by a predictable amount, or at all. There are several potential explanations for this finding.

All simulations are identical during the first 80 min of simulation. After this time, small differences begin to emerge. However, the storms do not interact with the city until approximately 70 min later. The most likely cause of these early differences is that some of the inflow air that enters the storm first passes over the idealized city. Analysis of the forward-integrated parcel trajectories reveals that at $t = 60$ min, when all simulations produce identical storms, air that enters the updraft originates to the left of the idealized cities (not shown). By $t = 100$ min, when differences between the simulations have emerged, a portion of the parcels originate over and to the right of the idealized cities (Figure 20). As heat islands of different magnitude develop across the range of simulations, the parcels that pass over the idealized cities will have slightly different temperature, humidity, and wind speed values between the simulations. It is likely that this thermodynamic variability leads to differences in fields such as vertical velocity (see Figure 3) and hydrometeor growth rates (see Figures 16 and 17) well before the storms pass over the idealized city. Even during quasi-steady periods, the updraft experiences oscillations due to the continual generation and decay of new cells at the leading edge of the cold pool (see Figure 3). Fovell and Ogura [42] showed that the frequency of this oscillation can be influenced by microphysical processes. Thus, it is possible that thermodynamic variability within the inflow

parcels alters the frequency of the intensification/decay cycle between the simulations. This shift in frequency could impact interpretation of the results when analyzing simulations at a common time and may explain why stronger heat islands do not always indicate stronger storm modification in the analysis presented.

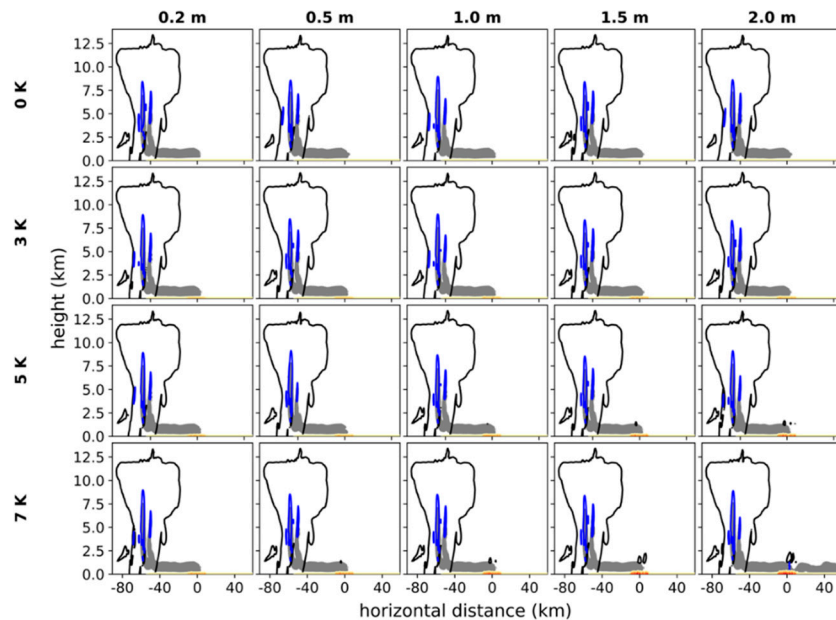


Figure 20. Evolution of parcel trajectories entering the storm updraft. The gray lines indicate parcel positions from the start of the simulation through 100 min, the solid black contour represents the hydrometeor mixing ratio of 0.02 g kg^{-1} at $t = 100 \text{ min}$, and the blue line is the 5 m s^{-1} contour of vertical velocity at $t = 100 \text{ min}$. Temperature at $t = 100 \text{ min}$ is contoured from 299 K (yellow) to 305 K (red) with a spacing of 0.5 K.

A second possibility is related to ‘chaos seeding’ as discussed by Ancell et al. [43]. It is possible that changes to the idealized city generate fast-moving high-frequency waves induced by a numerical roundoff error. These waves result in alterations to the storm structure and lead to non-physical results. While the presence of these waves cannot be completely dismissed, there are a few reasons why they are unlikely to have a significant impact on the results. First, the idealized simulations presented here are of a much shorter duration than those discussed by Ancell et al. [43]. They note that significant changes can be induced “within a day” whereas in the current suite of simulations, the focus is on the structure of the storms after only 2–3 h of integration time. Second, as discussed above, differences between the simulations begin to arise only after the storms ingest air parcels that originate from regions in the domain where the perturbations were placed. Finally, Ancell et al. [43] list several techniques to determine the physical validity of results from perturbation experiments. One such suggestion is to perform a regression analysis of input/response features from an ensemble of simulations. In the context of the current work, it was shown that increasing both the magnitude of the skin temperature perturbation as well as the horizontal z_0 gradient increases the depth and magnitude of the urban heat island. In general, the simulations with the stronger heat islands tended to yield the strongest response in terms of the parameters analyzed (updraft strength, graupel mixing ratio, upward mass flux, 10-m wind speed, etc.), but not always. For example, Figure 13, displays the distribution of buoyant acceleration along parcels entering the storm updraft after interaction with the idealized city. In general, increasing the surface z_0 gradient (while leaving the surface temperature unchanged) or increasing the surface temperature (while leaving the surface z_0 gradient unchanged) leads to an increase in the occurrence of larger buoyant accelerations. Two exceptions to this trend are

seen when comparing the 3Kz0.2 simulation to the 3Kz0.5 simulation, and the 3Kz0.2 simulation to the 5Kz0.2 simulation.

An additional exception can be seen in the three simulations with the strongest heat islands (5Kz2.0, 7Kz1.5, and 7Kz2.0). These simulations tend to exhibit a smaller degree of storm modification compared to other simulations with weaker heat islands. In these simulations, deep convection was initiated ahead of the main squall line on the downwind side of the idealized city (e.g., Figures 5, 6 and 11). It is possible that the interaction with this new convection weakened the updraft of the main squall line. Figures 10 and 11 indicate that a portion of the air entering the updraft of the main line originated in what should be the cold pool of the new developing convection. Inflow air that travels through these cold pools may have reduced temperature (and potential buoyancy), resulting in slightly weaker updrafts, reduced graupel mass, and weaker 10-m winds than would have occurred if the city-initiated convection did not exist. An additional 7Kz2.0 simulation (not shown) was completed using the same thermodynamic profile, except it was modified so that it contained a capping inversion [44]. In this simulation, new convection was not initiated downwind of the idealized city. Additional work is needed to determine if the results from this current study are valid across a range of convective environments.

5. Conclusions

The purpose of this work was to simulate city-storm interactions and identify the city characteristics most responsible for structural changes within the storm. To achieve this goal, a suite of idealized two-dimensional simulations was performed in which a simplified representation of a city was inserted into the center of the model domain. In each simulation, the surface temperature and/or surface roughness length within the idealized city were systematically increased relative to the surrounding area by some defined value. While the initial goal was to isolate these two effects, the results show that, in many ways, these two processes work together to decrease low-level stability and promote more vigorous storm updrafts. For example, while increasing the surface temperature over the city does produce a signature similar to an urban heat island, the magnitude and depth of the heat island signature increases with increasing z_0 within the city. In other words, not only does the z_0 gradient have a direct impact on winds, it also increases vertical mixing over the city to create a stronger and deeper urban heat island.

The simulations with the largest heat islands—those with the largest surface temperature and largest roughness gradient—had larger surface-based CAPE and smaller CIN over the idealized city. Compared to the control simulation, the storms in the simulations with heat islands tended to strengthen after they passed over the idealized city. Not only did updrafts become more vigorous, but they became larger, as evident by the increase in cloud top vertical perturbation pressure gradient force as well as the substantial increase in updraft mass flux—an increase that was considerably larger than the observed increase in maximum vertical velocity between simulations.

Interaction with the idealized city also had a strong impact on microphysical processes and near-surface winds. While the storm in the control simulation did experience an increase in graupel mass, the storms in the heat island simulations exhibited a much more substantial increase in graupel during and after interaction with the city. In many cases, modification to the storm structure was not confined to the time period of interaction with the idealized city. Increases in graupel/hail mass, and 10-m wind speeds persisted for more than 30 min after the storms passed over the city. However, the results of the parameter space experiments were neither linear nor monotonic. Increasing the magnitude of the heat island feature did not always lead to a more substantial storm modification. This likely indicates the presence of nonlinear feedback between the environment and in-storm processes. Future work will focus on exploring these feedbacks as well as expanding the simulations to three dimensions.

Funding: A portion of this research was funded by the National Science Foundation, grant number AGS-1953791.

Conflicts of Interest: The author declares no conflict of interest.

References

1. U.S. Census Bureau. Life Off the Highway: A Snapshot of Rural America. 2016. Available online: https://www.census.gov/newsroom/blogs/random-samplings/2016/12/life_off_the_highway.html (accessed on 30 March 2020).
2. United Nations. Available online: <https://www.un.org/development/desa/en/news/population/2018-revision-of-world-urbanization-prospects.html> (accessed on 30 March 2020).
3. Changnon, A.S.; Huff, F.A.; Semonin, R.G. METROMEX: An investigation of inadvertent weather modification. *Bull. Am. Meteorol. Soc.* **1971**, *52*, 958–968. [[CrossRef](#)]
4. Huff, F.A.; Changnon, S.A. Climatological assessment of urban effects on precipitation at St. Louis. *J. Appl. Meteorol.* **1972**, *11*, 823–842. [[CrossRef](#)]
5. Changnon, S.A.; Semonin, R.G.; Huff, F.A. Hypothesis for urban rainfall anomalies. *J. Appl. Meteorol.* **1976**, *15*, 544–560. [[CrossRef](#)]
6. Changnon, S.A.; Westcott, N.E. Heavy rainstorms in Chicago: Increasing frequency, altered impacts, and future implications. *J. Amer. Water Res. Assoc.* **2002**, *38*, 1467–1475. [[CrossRef](#)]
7. Shepherd, J.M.; Pierce, H. Rainfall modification by major urban areas: Observations from spaceborne rain radar on the TRMM satellite. *J. Appl. Meteorol.* **2002**, *41*, 689–701. [[CrossRef](#)]
8. Hand, L.M.; Shepherd, J.M. An investigation of warm-season spatial rainfall variability in Oklahoma City: Possible linkages to urbanization and prevailing wind. *J. Appl. Meteorol. Clim.* **2009**, *48*, 251–269. [[CrossRef](#)]
9. Dixon, P.G.; Mote, T.L. Patterns and causes of Atlanta’s urban heat island-initiated precipitation. *J. Appl. Meteorol.* **2003**, *42*, 1273–1284. [[CrossRef](#)]
10. Niyogi, D.; Pyle, P.; Lei, M.; Arya, S.P.; Kishtawal, C.M.; Shepherd, M.; Chen, F.; Wolfe, B. Urban modification of thunderstorms: An observational storm climatology and model case study for the Indianapolis urban region. *J. Appl. Meteorol. Climatol.* **2011**, *50*, 1129–1144. [[CrossRef](#)]
11. Ganeshan, M.; Murtugudde, R.; Imhoff, M.L. A multi-city analysis of the UHI-influence on warm season rainfall. *Urban Clim.* **2013**, *6*, 1–23. [[CrossRef](#)]
12. Burian, S.J.; Shepherd, J.M. Effect of urbanization on the diurnal rainfall pattern in Houston. *Hydrol. Process.* **2005**, *19*, 1089–1103. [[CrossRef](#)]
13. Mote, T.L.; Lacke, M.C.; Shepherd, J.M. Radar signatures of the urban effect on precipitation distribution: A case study for Atlanta, Georgia. *Geophys. Res. Lett.* **2007**, *34*, 2–5. [[CrossRef](#)]
14. Shem, W.; Shepherd, M. On the impact of urbanization on summertime thunderstorms in Atlanta: Two numerical model case studies. *Atmos. Res.* **2009**, *92*, 172–189. [[CrossRef](#)]
15. Bentley, M.L.; Stallins, J.A.; Ashley, W.S. Synoptic environments favourable for urban convection in Atlanta, Georgia. *Int. J. Clim.* **2012**, *32*, 1287–1294. [[CrossRef](#)]
16. Haberlie, A.M.; Ashley, W.S.; Pingel, T.J. The effect of urbanisation on the climatology of thunderstorm initiation. *Q. J. R. Meteorol. Soc.* **2015**, *141*, 663–675. [[CrossRef](#)]
17. Reames, L.J.; Stensrud, D.J. Influence of a Great Plains urban environment on a simulated supercell. *Mon. Weather Rev.* **2018**, 1437–1462. [[CrossRef](#)]
18. Naylor, J.; Sexton, A. The relationship between severe weather warnings, storm reports, and storm cell frequency in and around several large metropolitan areas. *Weather. Forecast.* **2018**, *33*, 1339–1358. [[CrossRef](#)]
19. Huff, F.A.; Changnon, S.A. Precipitation modification by major urban areas. *Bull. Am. Meteorol. Soc.* **1973**, *54*, 1220–1232. [[CrossRef](#)]
20. Braham, R.R.; Semonin, R.G.; Auer, A.H.; Changnon, S.A. Summary of urban effects on cloud and rain. In *Metromex: A Review and Summary. Meteorological Monographs*; Changnon, S.A., Ed.; American Meteorological Society: Boston, MA, USA, 1981; Volume 18, pp. 141–152.
21. Craig, K.J.; Bornstein, R.D. MM5 simulations of urban induced convective precipitation over Atlanta. In Proceedings of the 4th AMS Symposium on the Urban Environment, Norfolk, VA, USA, 19–24 May 2002; p. 38803.
22. Bornstein, R.; LeRoy, M. Urban barrier effects on convective and frontal thunderstorms. In Proceedings of the Fourth AMS Conference on Mesoscale Processes, Boulder, CO, USA, 25–29 June 1990.

23. Thielen, J.; Wobrock, W.; Gadian, A.; Mestayer, P.G.; Creutin, J.D. The possible influence of urban surfaces on rainfall development: A sensitivity study in 2D in the meso- γ -scale. *Atmos. Res.* **2000**, *54*, 15–39. [[CrossRef](#)]
24. van den Heever, S.C.; Cotton, W.R. Urban aerosol impacts on downwind convective storms. *J. Appl. Meteorol. Clim.* **2007**, *46*, 828–850. [[CrossRef](#)]
25. Ochoa, C.A.; Quintanar, A.I.; Raga, G.B.; Baumgardner, D. Changes in intense precipitation events in Mexico City. *J. Hydrometeorol.* **2015**. [[CrossRef](#)]
26. Stallins, J.A.; Carpenter, J.; Bentley, M.L.; Ashley, W.S.; Mulholland, J.A. Weekend-weekday aerosols and geographic variability in cloud-to-ground lightning for the urban region of Atlanta, Georgia, USA. *Reg. Environ. Chang.* **2013**, *13*, 137–151. [[CrossRef](#)]
27. Rozoff, C.M.; Cotton, W.R.; Adegoke, J.O. Simulation of St. Louis, Missouri, land use impacts on thunderstorms. *J. Appl. Meteorol.* **2013**, *42*, 716–738. [[CrossRef](#)]
28. Weisman, M.L.; Klemp, J.B. The dependence of numerically simulated convective storms on vertical wind shear and buoyancy. *Mon. Weather Rev.* **1982**, *110*, 504–520. [[CrossRef](#)]
29. Weisman, M.L.; Klemp, J.B. The structure and classification of numerically simulated convective storms in directionally varying wind shears. *Mon. Weather Rev.* **1984**, *112*, 2479–2498. [[CrossRef](#)]
30. Rotunno, R.; Klemp, J.B.; Weisman, M.L. A theory for strong, long-lived squall lines. *J. Atmos. Sci.* **1988**, *45*, 463–485. [[CrossRef](#)]
31. Fovell, R.G.; Ogura, Y. Effect of vertical wind shear on numerically simulated multicell storm structure. *J. Atmos. Sci.* **1989**, *46*, 3144–3176. [[CrossRef](#)]
32. Naylor, J.; Gilmore, M.S. Vorticity evolution leading to tornadogenesis and tornadogenesis failure in simulated supercells. *J. Atmos. Sci.* **2014**, *71*, 1201–1217. [[CrossRef](#)]
33. Lombardo, K.; Kading, T. The behavior of squall lines in horizontally heterogeneous coastal environments. *J. Atmos. Sci.* **2018**, *75*, 1243–1269. [[CrossRef](#)]
34. Bryan, G.H.; Fritsch, J.M. A benchmark simulation for moist nonhydrostatic numerical models. *Mon. Weather Rev.* **2002**, *130*, 2917–2928. [[CrossRef](#)]
35. Thompson, G.; Field, P.R.; Rasmussen, R.M.; Hall, W.D. Explicit forecasts of winter precipitation using an improved bulk microphysics scheme. Part II: Implementation of a new snow parameterization. *Mon. Weather Rev.* **2008**, *136*, 5095–5115. [[CrossRef](#)]
36. Tyson, P.D.; Toit, W.J.F.D.; Fuggle, R.F. Temperature structure above cities: Review and preliminary findings from the Johannesburg Urban Heat Island Project. *Atmos. Environ.* **1972**, *6*, 533–542. [[CrossRef](#)]
37. Oke, T.R. The Heat Island of the Urban Boundary Layer: Characteristics, Causes and Effects. In *Wind Climate in Cities*; Cermak, J.E., Davenport, A.G., Plate, E.J., Viegas, D.X., Eds.; Springer: Dordrecht, The Netherlands, 1995; pp. 81–107. [[CrossRef](#)]
38. Yuter, S.E.; Houze, R.A. Three-dimensional kinematic and microphysical evolution of Florida cumulonimbus. Part II: Frequency distributions of vertical velocity, reflectivity, and differential reflectivity. *Mon. Weather Rev.* **1995**, *123*, 1941–1963. [[CrossRef](#)]
39. Schlesinger, R.E. Effects of the pressure perturbation field in numerical models of unidirectionally sheared thunderstorm convection: Two versus three dimensions. *J. Atmos. Sci.* **1984**, *41*, 1571–1587. [[CrossRef](#)]
40. Peters, J.M. The impact of effective buoyancy and dynamic pressure forcing on vertical velocities within two-dimensional updrafts. *J. Atmos. Sci.* **2016**, *73*, 4531–4551. [[CrossRef](#)]
41. Morrison, H. Impacts of updraft size and dimensionality on the perturbation pressure and vertical velocity in cumulus convection. Part II: Comparison of theoretical and numerical solutions and fully dynamical simulations. *J. Atmos. Sci.* **2016**, *73*, 1455–1480. [[CrossRef](#)]
42. Fovell, R.G.; Ogura, Y. Numerical simulation of a midlatitude squall line in two dimensions. *J. Atmos. Sci.* **1988**, *45*, 3846–3879. [[CrossRef](#)]
43. Ancell, B.C.; Bogusz, A.; Lauridsen, M.J.; Nauert, C.J. Seeding chaos: The dire consequences of numerical noise in NWP perturbation experiments. *Bull. Am. Meteorol. Soc.* **2018**, *99*, 615–628. [[CrossRef](#)]
44. Naylor, J.; Askelson, M.A.; Gilmore, M.S. Influence of low-Level thermodynamic structure on the downdraft properties of simulated supercells. *Mon. Weather Rev.* **2012**, *140*, 2575–2589. [[CrossRef](#)]

